ELSEVIER

Materials Science and Engineering A333 (2002) 320–335

MATERIALS SCIENCE & ENGINEERING A

www.elsevier.com/locate/msea

Modeling and real time mapping of phases during GTA welding of 1005 steel

W. Zhang [a], J.W. Elmer [b], T. DebRoy [a,*]

[a] *Department of Material Science and Engineering, The Pennsylvania State University, University Park, PA 16802-5006, USA*
[b] *Chemistry and Materials Science Department, Lawrence Livermore National Laboratory, Livermore, CA 94551, USA*

Received 13 August 2001; received in revised form 15 October 2001

Abstract

Evolution of the microstructure in AISI 1005 steel weldments was studied during gas tungsten arc (GTA) welding experimentally and theoretically. The experimental work involved real-time mapping of phases in the heat-affected zone (HAZ) using a synchrotron-based spatially resolved X-ray diffraction (SRXRD) technique and post weld microstructural characterization of the fusion zone (FZ). A three-dimensional heat transfer and fluid flow model was used to calculate the temperature and velocity fields, thermal cycles, and the geometry of the FZ and the HAZ. The experimental SRXRD phase map and the computed thermal cycles were used to determine the kinetic parameters in the Johnson–Mehl–Avrami (JMA) equation for the ferrite to austenite transformation during heating in the HAZ. Apart from providing a quantitative expression for the kinetics of this transformation, the results are consistent with a decreasing nucleation rate of austenite from a ferrite matrix with time. In the FZ, the volume fractions of microconstituents were calculated using an existing phase transformation model and the computed thermal cycles. Good agreement was found between the calculated and experimental volume fractions of allotriomorphic and Widmanstatten ferrites in the FZ. The results indicate significant promise for understanding microstructure evolution during GTA welding of AISI 1005 steel by a combination of real time phase mapping and modeling.

Keywords: Phase transformations; 1005 steel; JMA kinetics; X-ray diffraction; Heat transfer and fluid flow; GTA welding

---

1. Introduction

During welding, the interaction of the heat source and the material leads to rapid heating, melting and the formation of the weld pool. In the weld pool, the molten metal undergoes strong recirculation and the flow of liquid metal significantly affects the temperature fields, thermal cycles and the weld pool geometry. When the heat source moves away, the weld pool cools and eventually solidifies. As the temperature drops, various solid-state phase transformations take place resulting in the final microstructure of the weldment [1–3]. The properties of a weldment, such as strength, ductility, toughness, and corrosion resistance are significantly affected by its microstructure. Thus, it is important to understand the microstructure evolution during welding.

A series of phase transformations take place in both the fusion zone (FZ) and the heat-affected zone (HAZ) during welding of low carbon steels. The microstructural history of the FZ is α-ferrite $\rightarrow$ γ-austenite $\rightarrow$ δ-ferrite $\rightarrow$ liquid $\rightarrow$ δ-ferrite $\rightarrow$ γ-austenite $\rightarrow$ α-ferrite, while the typical microstructure evolution in the HAZ corresponds to α-ferrite $\rightarrow$ γ-austenite $\rightarrow$ α-ferrite. In the HAZ, the $\alpha \rightarrow \gamma$ transformation during heating is of importance because the grain size, phase fraction and concentration homogeneity of transformed γ phase affects the kinetics of subsequent γ grain growth and phase transformations during cooling [4,5]. On the other hand, the weld integrity and performance are largely affected by the solidification transformation in the FZ. However, the final microstructure in the weldment is fairly complex because the solid-state $\gamma \rightarrow \alpha$ transformation can significantly alter the solidification microstructure [1–3,6]. Therefore, during welding of low carbon steels, the $\alpha \rightarrow \gamma$ transformation in the HAZ during heating and the reverse $\gamma \rightarrow \alpha$ transformation in the FZ and HAZ during cooling are very important.

---

* Corresponding author. Tel.: + 1-814-865-1974; fax: + 1-814-865-2917.
E-mail address: debroy@psu.edu (T. DebRoy).

0921-5093/02/$ - see front matter © 2002 Elsevier Science B.V. All rights reserved.
PII: S0921-5093(01)01857-3

While the need for better understanding of the phase transformation kinetics is well recognized, the use of conventional methods, such as dilatometry [7], to study the phase transformation kinetics during welding is inherently difficult. First, the conventional methods are indirect in that they measure a certain change in the welded sample (e.g. changes in length) and cannot directly determine the phases present during the test. Furthermore, these methods can only provide phase transformation data for heating and cooling rates on the order of 1 K s^{-1}, which is much less than those of arc, laser and electron beam welds [8]. A recently developed Spatially resolved X-ray diffraction (SRXRD) technique using synchrotron radiation can largely overcome those difficulties. During welding of steels, partial and complete transformations to α-ferrite, γ-austenite, and δ-ferrite phase regions have been identified using this technique with sufficient spatial resolution to identify the location of these phase fields [9,10]. Thus, this newly developed technique is useful to investigate phase transformations during welding of steels.

Since phase transformations in the weldment take place during heating and cooling, knowledge of the weld thermal cycles is a prerequisite for understanding microstructure evolution during welding. Measurement of temperature profiles in the weldment still remains a major challenge today. Although some progress has been made in the measurement of weld pool surface temperatures, a unified reliable technique has not yet emerged. Measurement of temperature fields in the heat affected zone is time consuming and cumbersome. A practical recourse is to use a well-tested three-dimensional (3-D) numerical heat transfer and fluid flow model to obtain accurate transient temperature fields, peak temperatures and heating and cooling rates [11,12].

In the present research, by the combination of experiments and modeling, we seek to quantitatively understand the kinetics and mechanisms of $\alpha \rightarrow \gamma$ transformation during heating in the HAZ and $\gamma \rightarrow \alpha$ transformation during cooling in the FZ during gas tungsten arc (GTA) welding of AISI 1005 steel. The kinetic data of $\alpha \rightarrow \gamma$ transformation in the HAZ were determined from the real time phase map by SRXRD technique. Since this transformation involves nucleation and growth, the analysis of the kinetic data was based on a modified Johnson–Mehl–Avrami (JMA) equation considering non-isothermal behavior. The thermal cycles were computed from the 3-D heat transfer and fluid flow model. The JMA kinetic parameters for the $\alpha \rightarrow \gamma$ phase transformation in AISI 1005 steel were then determined from the combination of real time phase map and calculated thermal cycles. These kinetic parameters are useful to quantitatively describe the $\alpha \rightarrow \gamma$ phase transformation kinetics. Apart from contributing to the quantitative understanding of the phase transformation kinetics, these kinetic parameters also provide significant insight about the mechanism of austenite nucleation from the ferrite matrix.

The $\gamma \rightarrow \alpha$ transformation during cooling of the weld metal in the FZ has been examined by Bhadeshia et al. [13–15]. For a known cooling rate, their model can provide a quantitative description of the final microconstituents in the FZ resulting from the transformation of $\gamma \rightarrow \alpha$ transformation. Using the computed thermal cycles from the 3-D heat transfer and fluid flow model, the weld metal microstructure was calculated using their model. The computed volume percents of allotriomorphic and Widmanstatten ferrites were compared with the corresponding values determined by quantitative microscopy.

Quantitative understanding of both the $\alpha \rightarrow \gamma$ phase transformation during heating in the HAZ and the $\gamma \rightarrow \alpha$ transformation during cooling in the FZ represents a contribution to the growing quantitative knowledge base in fusion welding. Expansion of this knowledge base is necessary, if not essential, to make progress in understanding and controlling weldment microstructure and properties based on scientific principles.

2. Experimental procedure

2.1. Welding

AISI 1005 steel bar of 10.8 cm diameter was welded by GTA welding. The composition of the as received bar was (by wt.%): 0.05 C, 0.31 Mn, 0.18 Si, 0.11 Ni, 0.10 Cr, 0.009 P, 0.008 Cu, 0.005 S, <0.005 Al, <0.005 Nb, <0.005 Mo, <0.005 Ti and <0.005 V. GTA welds were made on steel bars using a constant power of 1.9 kW (110 A, 17.5 V) with a W-2%Th welding electrode measuring 4.7 mm in diameter. High purity (99.999%) helium was used as both the welding and shielding gases. The steel bar was rotated below the fixed electrode at a constant speed of 0.11 rpm, which corresponds to a surface welding speed of 0.6 mm s^{-1}. Additional details about the welding procedure are reported in the literature [10].

2.2. Spatially resolved X-ray diffraction

The salient features of the experiments are briefly described here. More details about the SRXRD setup are available in the literature [8–10]. The SRXRD measurements were performed on the 31-pole wiggler beam line at Stanford Synchrotron Radiation Laboratory (SSRL) with Stanford Positron–Electron Accumulation Ring (SPEAR) operating at an electron energy of 3.0 GeV and an injection current of ~ 100 mA. The focused monochromatic beam was passed through a

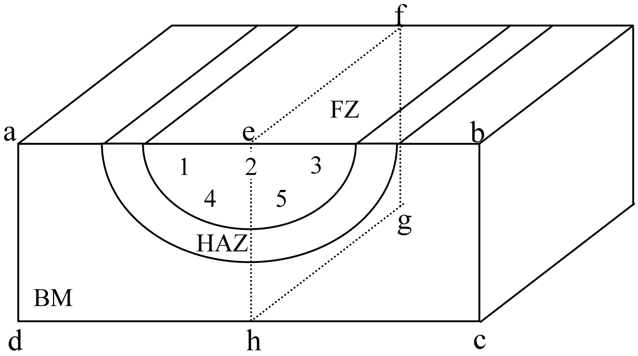

Fig. 1. Diagram showing the two sections where measurements were made. The welding direction is along the line ef. The plane abcd represents the transverse section, on which the quantitative point counting was carried out at the locations 1–5 to determine the volume fractions of microconstituents within the FZ. The plane efgh represents the longitudinal section, on which the prior austenite grain structure was examined.

260 μm tungsten pinhole to render a sub-millimeter beam on the sample at an incident angle of ~25°. The SRXRD patterns were recorded behind the weld using a 50 mm long 2048 element position sensitive Si photodiode array detector. The welding assembly was integrally mounted to a translation stage driven by a stepper motor with 10 μm precision and placed inside an environmentally controlled chamber to minimize oxidation during welding. SRXRD data were taken while the beam was at a fixed location with respect to the welding electrode and collected for 10 s while the bar rotated under the stationary torch at a constant speed.

2.3. Metallographic characterization

As shown in Fig. 1, the welded samples were sectioned transverse to the welding direction to examine microstructures. Fig. 2 shows the optical microstructure of base metal, which is composed of ferrite and small regions of pearlite. The HAZ consisted of a partially transformed region, a fine grained region and a coarse grained region [10] as shown in Fig. 3(a). The microstructure in the coarse grained region of the HAZ was composed of allotriomorphic and Widmanstatten ferrites, as shown in Fig. 3(b). The FZ microstructure was largely composed of allotriomorphic ferrite, Widmanstatten ferrite and small amount of other microconstituents, as shown in Fig. 4. Under a light microscope, allotriomorphic ferrite is usually equiaxed or lenticular in form and Widmanstatten ferrite has a thin wedge shape [16]. The point counting method was used following the International Institute of Welding (IIW) guidelines [17] to determine the relative quantities of these two ferrites in the FZ. As shown in Fig. 1, various locations within the FZ were examined. At each location, 100 points were counted to determine the volume fractions of microconstituents. The resulting volume fractions and their standard deviations are summarized in Table 1.

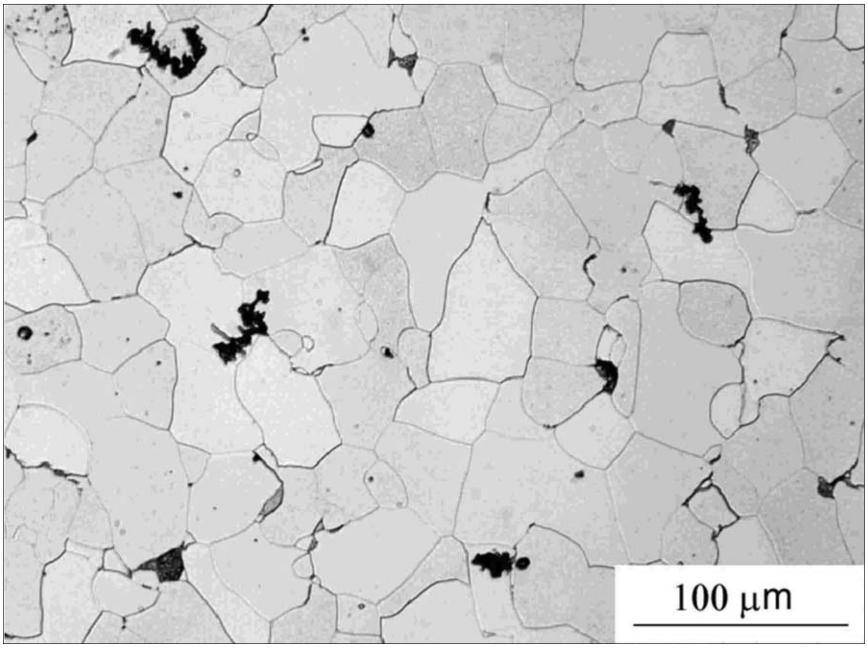

Fig. 2. Optical micrograph of AISI 1005 steel base metal, etched in 2% nital solution.

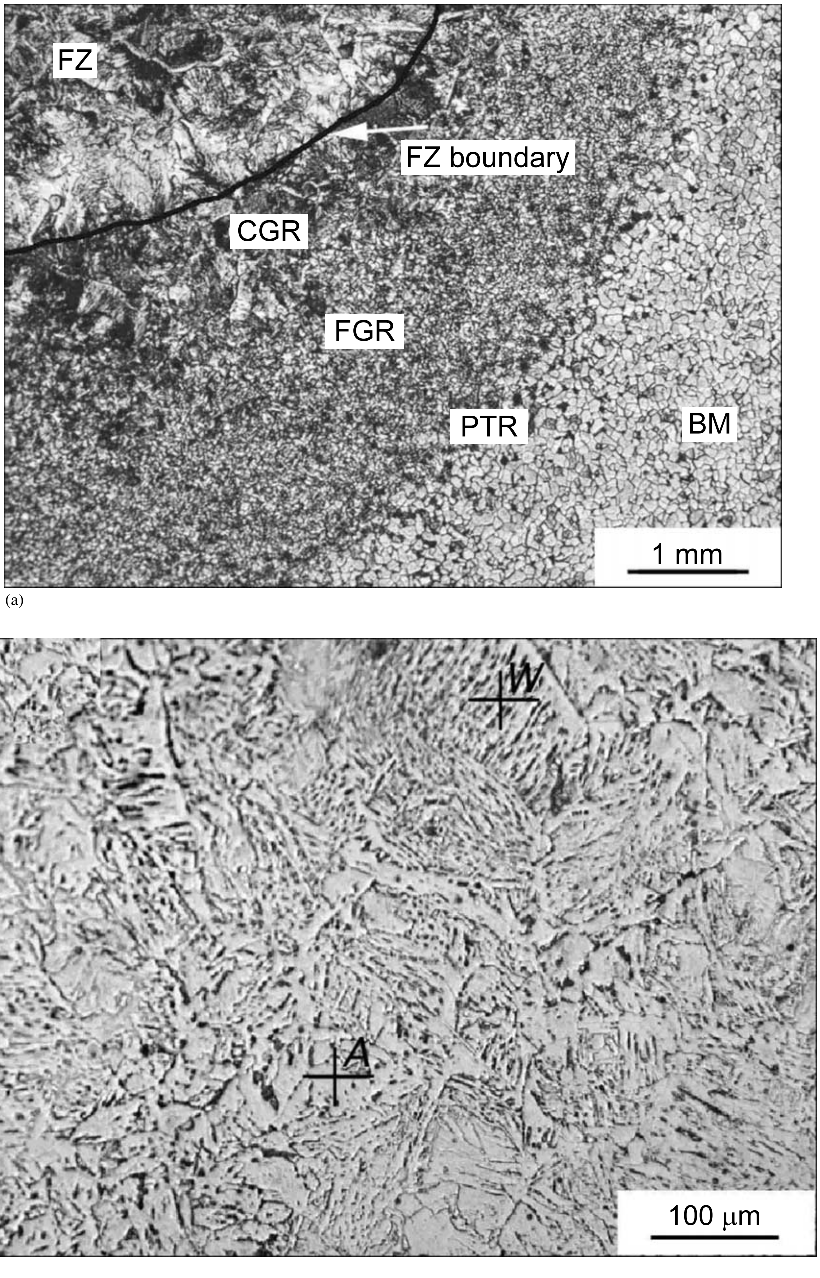

Fig. 3. (a) Macrostructure of the weldment, etched in 2% nital solution. The symbols FZ and BM represent FZ and base metal, respectively, and the symbols CGR, FGR and PTR represent the coarse grained region, fine grained region and partially transformed region, respectively. The HAZ consisted of the CGR, FGR, and PTR regions. (b) Microstructure of the coarse grained region in the HAZ etched in saturated picral solution [16]. The symbols A and W represent allotriomorphic ferrite and Widmanstatten ferrite, respectively.

3. Mathematical modeling

3.1. Calculation of heat transfer and fluid flow

The 3-D heat transfer and fluid flow model used in the present research has been extensively tested. Details about this model are available in the literature [11,12], only salient features are presented here. The transient problem was transformed into a steady-state problem by using a coordinate system moving with the heat source. The equations of conservation of mass, momentum and energy in 3-D form were discretized using the upwind scheme and numerically solved by the SIMPLER algorithm [18]. A 65 × 38 × 32 grid system was used in the calculation and the corresponding computational domain had dimensions of 287 mm in length, 57 mm in width and 41 mm in depth. The data used for the calculation of the fluid flow and heat transfer are presented in Table 2.

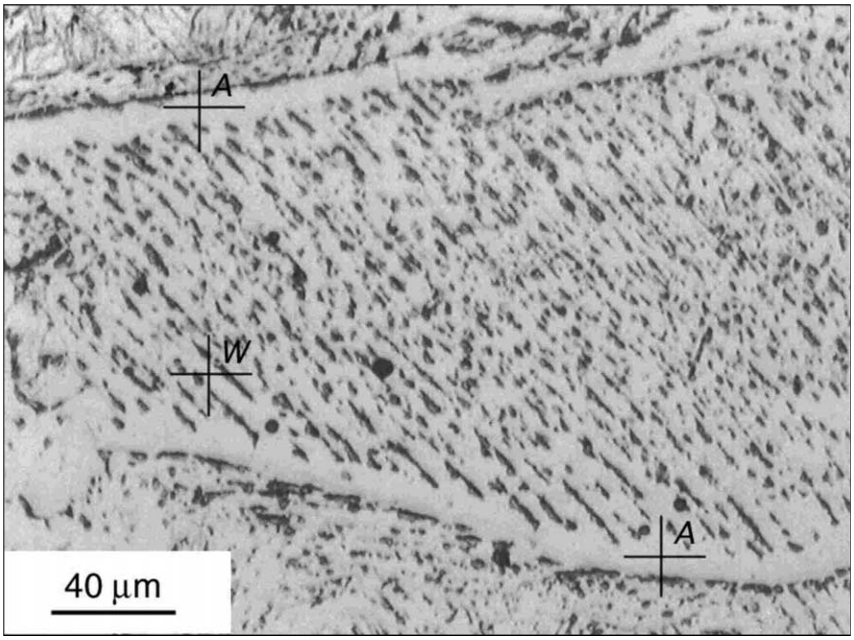

Fig. 4. Microstructure of the FZ, etched in saturated picral solution. The symbols A and W represent allotriomorphic ferrite and Widmanstatten ferrite, respectively.

Table 1
Experimentally measured volume fractions of microconstituents in the fusion zone

	Volume fractions at different locations (%)					Average volume fractions (%)	Standard deviation (%)
	1	2	3	4	5		
V_α	35	30	37	28	28	31.6	3.7
V_W	57	56	59	62	61	59	2.2
V_o	8	14	4	10	11	9.4	3.3

Locations 1–5 are shown in Fig. 1. The symbols V_α, V_W, and V_o represent the volume fractions of allotriomorphic ferrite, Widmanstatten ferrite and other microconstituents, respectively.

3.2. Calculation of thermal cycles

After obtaining the steady-state temperature field, the thermal cycle at any given location (x, y, z) was calculated using the following equation:

$$T(x, y, z, t_2) = \frac{T_S(\zeta_2, y, z) - T_S(\zeta_1, y, z)}{\zeta_2 - \zeta_1} V_S(t_2 - t_1) + T(x, y, z, t_1) \tag{1}$$

where $T(x, y, z, t_2)$ and $T(x, y, z, t_1)$ are the temperatures at time t_2 and t_1, respectively, $T_s(\xi_2, y, z)$ and $T_s(\xi_1, y, z)$ are the steady-state temperatures at coordinates (ξ_2, y, z) and (ξ_1, y, z), respectively, V_s is the welding speed and $(\xi_2 - \xi_1)$ is the length welded in time $(t_2 - t_1)$.

Table 2
Data used for the calculation of velocity and temperature fields

Physical property	Value
Liquidus temperature (K)	1802
Solidus temperature (K)	1779
Density of liquid metal (kg m^{-3})	7.87×10^3
Viscosity of liquid (kg m^{-1} s^{-1})	6.3×10^{-3}
Thermal conductivity of solid (J m^{-1} s^{-1} K^{-1})	36.4
Thermal conductivity of liquid (J m^{-1} s^{-1} K^{-1})	36.4
Specific heat of solid (J kg^{-1} K^{-1})	754
Specific heat of liquid (J kg^{-1} K^{-1})	754
Latent heat of melting (J kg^{-1})	2.7×10^5
Temperature coefficient of surface tension (N m^{-1} K^{-1})	-0.49×10^{-3}

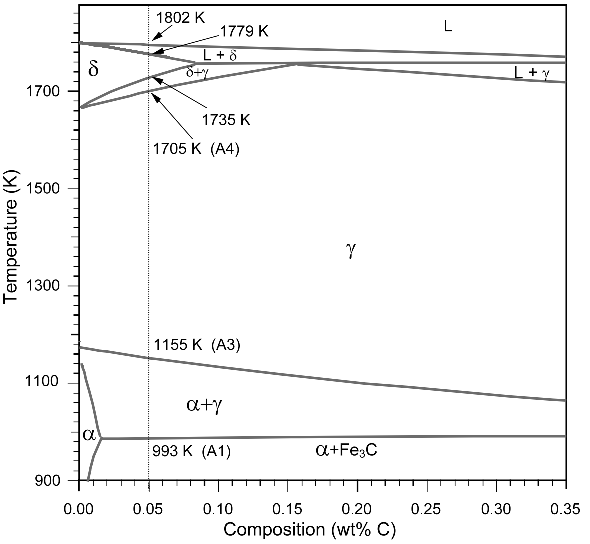

Fig. 5. Calculated pseudo-binary Fe–C phase diagram for the AISI 1005 steel (adapted from [10]).

3.3. Calculation of phase transformations

3.3.1. Phase equilibria

The pseudo-binary Fe–C diagram [10] for AISI 1005 steel is illustrated in Fig. 5. On slow heating, the dissolution of carbides and formation of γ take place at 993 K, producing a mixture of α and γ. The α phase transforms completely to γ at 1155 K. The δ phase begins to form at 1705 K and coexists with γ up to 1735 K where γ completely transforms to δ. At 1779 K δ starts to melt and it is completely converted to liquid at 1802 K. On slow cooling, the phase transformations occur in the reverse order.

3.3.2. JMA equation for $\alpha \rightarrow \gamma$ transformation during heating

In the HAZ, the $\alpha \rightarrow \gamma$ phase transformation in low alloy steels involves the nucleation of γ phase from the α matrix and the growth of γ phase by diffusion [19–24]. Therefore, JMA equation is applicable to describe the $\alpha \rightarrow \gamma$ phase transformation in AISI 1005 steel. At a constant temperature, the JMA equation can be expressed as [25]:

$$f = 1 - \exp[-\{k(T) \times t\}^n] \tag{2}$$

where f is the phase fraction of transformed γ, t is the time. The JMA time exponent n is a constant independent of temperature. Its value is determined by the nucleation and growth mechanism. The rate factor $k(T)$, which is related to the nucleation and growth rate, is a function of temperature and can be calculated by the Arrhenius equation:

$$k(T) = k_0 \times \exp\left(-\frac{Q}{RT}\right) \tag{3}$$

In Eq. (3), Q is the activation energy of the $\alpha \rightarrow \gamma$ transformation involving nucleation and growth of γ phase, k_0 is the pre-exponential constant, R is the universal gas constant and T is the absolute temperature. The values of $k(T)$, Q and k_0 are usually determined by isothermal experiments. Under non-isothermal conditions, the JMA equation can be modified as:

$$\begin{aligned} f(t(T_\mathrm{m})) &= 1 - \exp\left[-\left\{\sum_{i=1}^{m} k(T_i) \times \Delta t\right\}^n\right] \\ &= 1 - \exp\left[-\left\{\sum_{i=1}^{m} k_0 \times \exp\left(-\frac{Q}{RT_i}\right) \times \Delta t\right\}^n\right] \end{aligned} \tag{4}$$

where f stands for the transformed γ phase fraction, Δt is the time step, T_i is the temperature at time $i\Delta t$, and the symbol m indicates the number of time steps [25,26].

3.3.3. Transformation of austenite during cooling

In low alloy steels, allotriomorphic ferrite is the first phase to form from the γ phase during cooling of the weld metal. It nucleates along the γ grain boundaries and grows by diffusion [13–15]. As the temperature decreases, the growth rate of allotriomorphic ferrite decreases, and it finally gives way to the growth of Widmanstatten ferrite. Widmanstatten ferrite nucleates either directly from the austenite grain surfaces or indirectly from allotriomorphic ferrite/austenite interfaces [3,6]. It grows by a combination of carbon diffusion and an invariant-plane strain (IPS) shape change [3,6]. At even lower temperatures, the untransformed austenite completely transforms into bainite or martensite depending on the cooling rate [13–15]. It should be noted that two or more transformations may occur simultaneously at certain temperatures and compete with each other.

Based on thermodynamics and phase transformation kinetics, the TTT and CCT diagrams and the volume fractions of weld metal microstructures can be calculated using an available phase transformation model and the computed cooling rates. The details of the model [13–15] and its recent applications [27,28] are available in the literature and the assumptions and the salient features are described in Appendix A. A flow chart of microstructure evolution during GTA welding of AISI 1005 steel by the combination of experiments and modeling is shown in Fig. 6.

4. Results and discussion

4.1. Temperature and velocity fields and weld pool geometry

The computed 3-D velocities and temperature fields are shown in Fig. 7(a and b), respectively. In these figures, the temperature field is indicated by the contour lines and the fluid velocities are represented by the arrows. The liquid metal motion in the weld pool is driven mainly by the surface tension and electromagnetic forces and, to a much lesser extent, by the buoyancy force. Due to the temperature coefficient of surface tension $d\gamma/dT$ has a negative value, the surface tension force drives the liquid metal from the center to the periphery at the surface of the weld pool. As a result of the outward liquid metal flow on the surface, the weld pool is wide and shallow. The temperature gradient in front of the heat source is somewhat higher than that behind the heat source. These temperature gradients result in slightly greater liquid metal velocities in front of the heat source than behind the heat source.

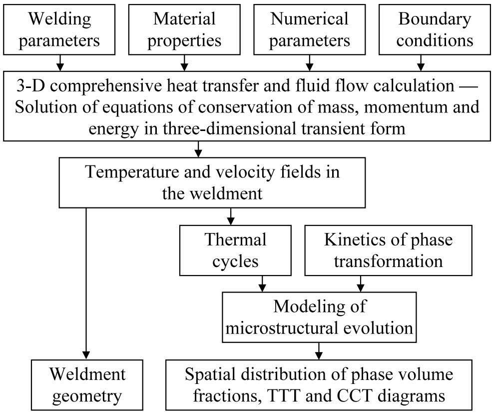

Fig. 6. Flow chart for the microstructure modeling scheme.

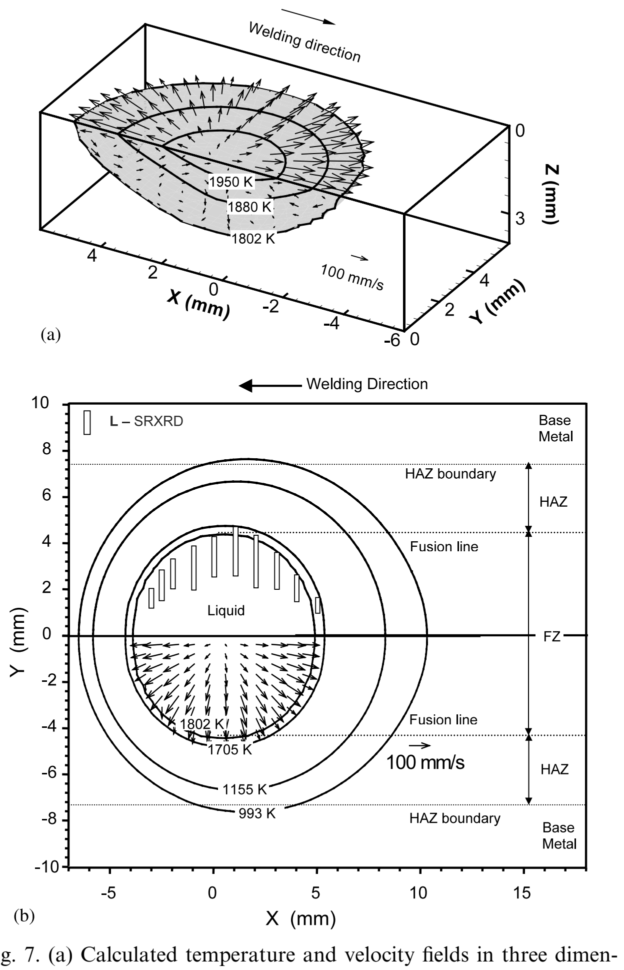

Fig. 7. (a) Calculated temperature and velocity fields in three dimensions. (b) Calculated temperature and velocity fields on the top surface. The weld pool boundary is represented by the 1802 K isotherm. The molten metal velocities are represented by the arrows and the velocities are located at the tail of the arrows. The liquid phase was plotted from the real time SRXRD data. The FZ and HAZ boundaries were measured on the metallographically prepared samples. The heat source is positioned at $x=y=0$ mm. Welding conditions, GTA, 110 A, 17.5 V; and 0.6 mm s^{-1} welding speed.

Fig. 7(b) shows the geometry of the weld pool based on SRXRD [10] and metallographic data. The FZ and HAZ boundaries, indicated by the horizontal dotted lines in the figure, were measured on the welded samples [10], while the superimposed isotherms were calculated from the 3-D comprehensive heat transfer and fluid flow model. The calculated liquidus isothermal line (1802 K) agrees well with the measured weld pool boundary, and the calculated eutectoid temperature profile (993 K) matches well with the metallographically determined HAZ boundary. The agreement between the calculated and experimental geometry indicates that the overall features of the FZ and HAZ in the GTA welds can be satisfactorily predicted by the model. Furthermore, the spatial distribution of peak temperatures, heating rates and cooling rates can be determined. Thermal cycles are necessary for understanding the evolution of microstructure in the weldment.

4.2. Thermal cycles

The spatial distribution of temperatures shown in Fig. 7 was converted into thermal cycles using Eq. (1). Considering temperatures along a line parallel to the welding direction (x-direction), the corresponding time values were obtained by dividing the x-distance by the welding speed. This conversion from distance to time coordinates is required to understand the welding induced phase transformations that are affected by both time and temperature. A series of thermal cycles is plotted in Fig. 8 for locations at different distances from the weld centerline. In this plot time equal to zero was arbitrarily selected to correspond to the heat source location identified in Fig. 7 as $x=0$. The peak temperature, the heating and cooling rates at various locations decrease with increasing distance from the welding centerline. Depending on the local temperatures, different phase transformations take place in the HAZ. For example, for a path parallel to the welding direction at $y=5.5$ mm from the weld centerline, the peak tempera-

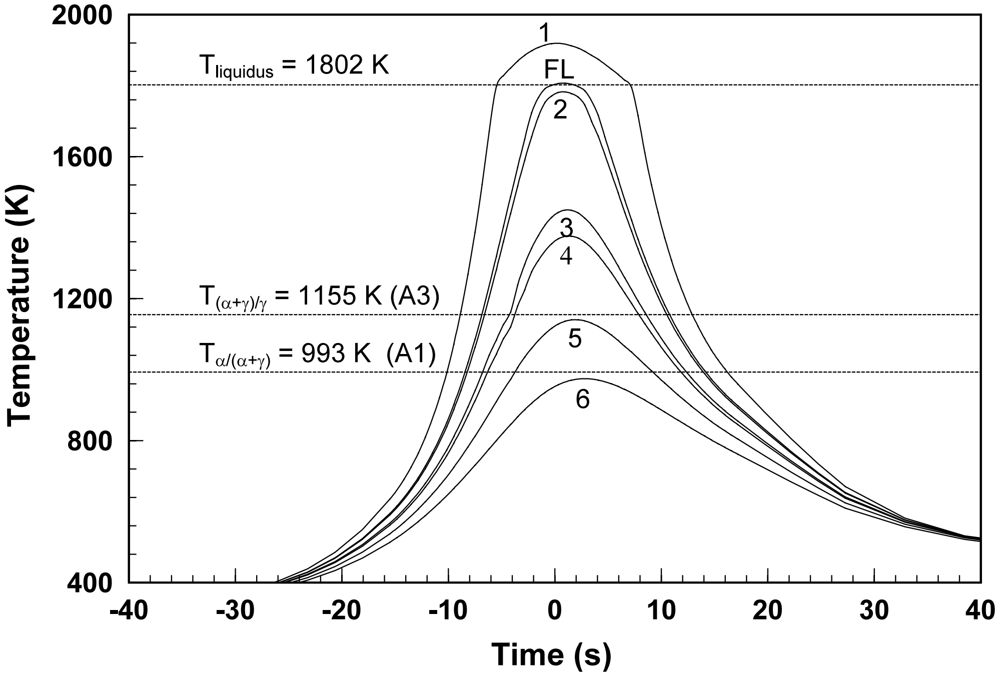

Fig. 8. Calculated thermal cycles at different locations. Distances from weld centerline: 1, 2.5 mm; 2, 4.5 mm; 3, 5.5 mm; 4, 5.75 mm; 5, 6.75 mm; 6, 7.8 mm; and FL, 4.4 mm. Time equal to zero was arbitrarily selected to correspond to the heat source location at $x = 0$ in Fig. 7.

ture and the time period over the A3 temperature (1155 K) is relatively large. As a result, this location experiences complete $\alpha \rightarrow \gamma$ transformation during heating, and the reverse $\gamma \rightarrow \alpha$ transformation during cooling. Further away from the weld centerline, at $y = 7.8$ mm, the peak temperature never reaches the A1 temperature (993 K), and therefore, does not experience the $\alpha \rightarrow \gamma$ transformation. Between these locations, the $\alpha \rightarrow \gamma$ transformation takes place under different heating rates and peak temperatures, which result in different extents of completion. Further analysis of kinetic data was undertaken to understand the $\alpha \rightarrow \gamma$ transformation during heating.

For low carbon steels, the $\gamma \rightarrow \alpha$ transformation during cooling usually occurs within the temperature range 1073–773 K (800–500 °C) [28]. In FZ, the cooling rates vary with position at high temperatures above the melting point. As the weld metal cools, the spatial variation of cooling rates in the FZ decreases. In the 1073–773 K range, the cooling rate in the FZ is almost independent of position, as shown in Fig. 9. This is due to the nearly constant outward heat loss from all locations within the FZ [28,29]. A consequence of this fact is that the spatial variation of microstructure within the FZ of arc welds is expected to be insignificant. The computed cooling rates and an available phase transformation model [13–15] were used to quantitatively understand the microstructure evolution in the FZ.

4.3. Phase transformations

4.3.1. Spatial distribution of phases in the HAZ

Fig. 10 shows the spatial phase distribution map determined from the SRXRD data [10]. This map assumes mirror symmetry of the weld about $y = 0$ plane where the stationary welding electrode is positioned at $x = y = 0$. The welded sample moves from left to right along the x direction under the stationary arc. Five phase regions were identified in Fig. 10, α region,

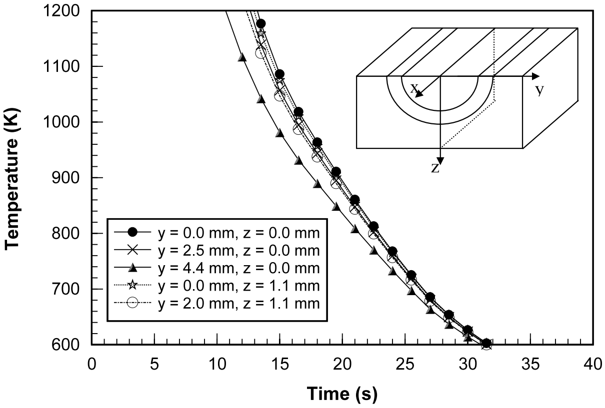

Fig. 9. Calculated cooling curves at different locations. The symbol y represents the distance from the weld centerline, while the symbol z represents the distance from the top surface, as shown in the small figure. Time zero corresponds to the heat source location at $x = 0$ mm in Fig. 7.

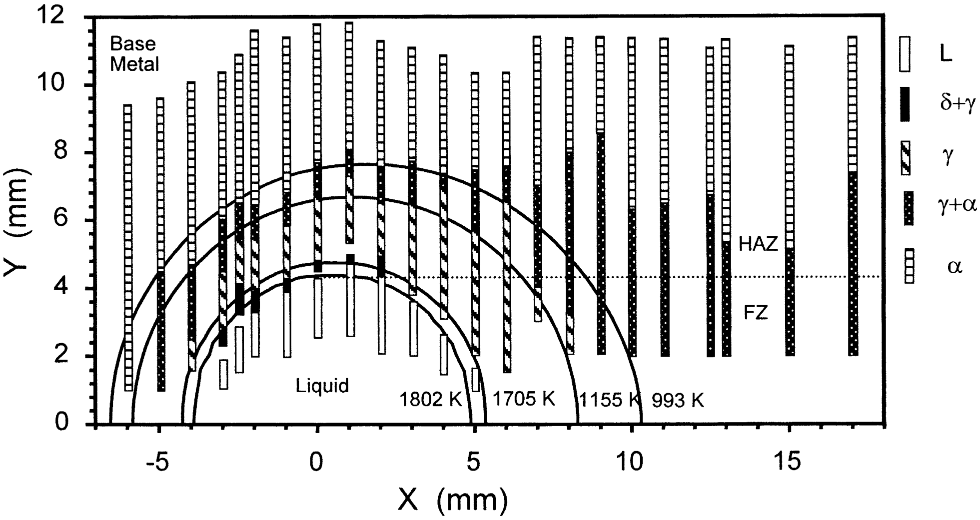

Fig. 10. Real-time SRXRD phase distribution maps. The superimposed isotherms were calculated from the 3-D heat transfer and fluid flow model.

$(\alpha+\gamma)$ two-phase region, single-phase γ region, $(\delta+\gamma)$ region and liquid region. The calculated isotherms of $\alpha/(\alpha+\gamma)$ (993 K), $(\alpha+\gamma)/\gamma$ (1155 K), $\gamma/(\delta+\gamma)$ (1705 K) and $(\delta+\gamma)$/liquid (1802 K) phase transformations are superimposed on the phase distribution map. It is observed that the calculated δ/liquid and $\alpha/(\alpha+\gamma)$ isotherms agree well with the liquid region and α region on the front (heating) side of the weld, respectively. Therefore, these phase boundaries can be reasonably predicted by the calculated isotherms. The prediction of the $(\alpha+\gamma)/\gamma$ boundary requires the knowledge of both thermal cycles and the kinetics of the transformation, and therefore, cannot be predicted by the thermal model alone.

4.3.2. $\alpha\rightarrow\gamma$ *transformation in the HAZ during heating*

The rate of the $\alpha\rightarrow\gamma$ transformation on heating can be expressed by the JMA equation since the transformation involves nucleation and growth of γ phase. Eq. (4) indicates that the JMA kinetic parameters (Q, k_0 and n) determine the rate of the $\alpha\rightarrow\gamma$ transformation. If the values of these three parameters can be specified, the rate of this phase transformation can be quantitatively described for various thermal cycles. Our goal is to determine these kinetic parameters for the AISI 1005 steel from the SRXRD phase distribution map and the computed temperature field. Apart from providing a quantitative basis for the calculation of the rate of $\alpha\rightarrow\gamma$ transformation in this steel, values of these kinetic parameters can provide insight about the nucleation mode of austenite in the ferrite matrix in the AISI 1005 steel.

In low alloy steels, the activation energy for the $\alpha\rightarrow\gamma$ transformation, Q, does not change significantly with the variation of carbon and alloy concentrations [23,24], and its value can be assumed to be comparable to that for the diffusion of carbon in the γ phase [23,24]. This value of the activation energy is consistent with the fact that the growth of γ phase is controlled by the diffusion of carbon atoms in the γ phase, i.e. diffusion-controlled growth [19–24]. The activation energy for this transformation in steels that have similar carbon and alloy concentrations (0.08 C, 0.45 Mn, 0.03 Si, 0.045 S and 0.04 P by wt.%) as the AISI 1005 steel has been reported in the literature as 117.07 kJ mol^{-1} [23]. This value of activation energy was used in the present investigation.

The values of n and k_0 for the $\alpha\rightarrow\gamma$ transformation in AISI 1005 steel depend largely on the starting microstructure and are not readily available. However, the SRXRD phase map and the computed thermal cycles can be used to calculate these parameters. This is done by linearizing the modified JMA equation, i.e. Eq. (4) representing the non-isothermal $\alpha\rightarrow\gamma$ transformation as follows:

$$\ln c = \ln\{-\ln(1-f)\} \tag{5}$$

where the symbol c is expressed by the following equation:

$$c=\left\{\sum_{i=1}^{m} k_0 \times \exp\left(-\frac{Q}{RT_i}\right) \times \Delta t\right\}^n = (k_0 s)^n \tag{6}$$

where the symbol s is expressed as:

$$s=\sum_{i=1}^{m} \Delta t \times \exp\left(-\frac{Q}{RT_i}\right) \tag{7}$$

Combining Eqs. (5) and (6) to eliminate c, we have:

$$\ln\{-\ln(1-f)\} = n \ln s + n \ln k_0 \tag{8}$$

Thus, the value of n can be obtained from the slope of a plot of $\ln\{-\ln(1-f)\}$ versus $\ln s$. Once the value of n is known, the value of k_0 can be calculated from the intercept of the plot as:

$$k_0 = \exp\left(\frac{b}{n}\right) \qquad (9)$$

where b is the intercept of this line with the $\ln\{-\ln(1-f)\}$ axis.

During welding, as the distance between the heat source and the monitoring line NS shown in Fig. 11 decreases, the temperatures at all points along this line increase. A portion of the temperature histories of points A through F on line NS are indicated in Fig. 11. Only the portion of the thermal cycle that contributed to the $\alpha \rightarrow \gamma$ transformation is shown. The lowest temperature for the transformation is assumed to be the A1 temperature. The maximum temperatures at various locations are the computed temperatures when the phase fractions were measured. These temperatures are indicated by the solid circles. The distance between the heat source and the monitoring line, NS, corresponds to a time of -4.17 s ($= -2.5$ mm/0.6 mm s^{-1}). The phase fractions of austenite along NS from $y = 5.25$–6.5 mm at $x = -2.5$ mm were determined from the SRXRD phase map, and are presented in Table 3 [10]. For each location indicated in Table 3, the value of s

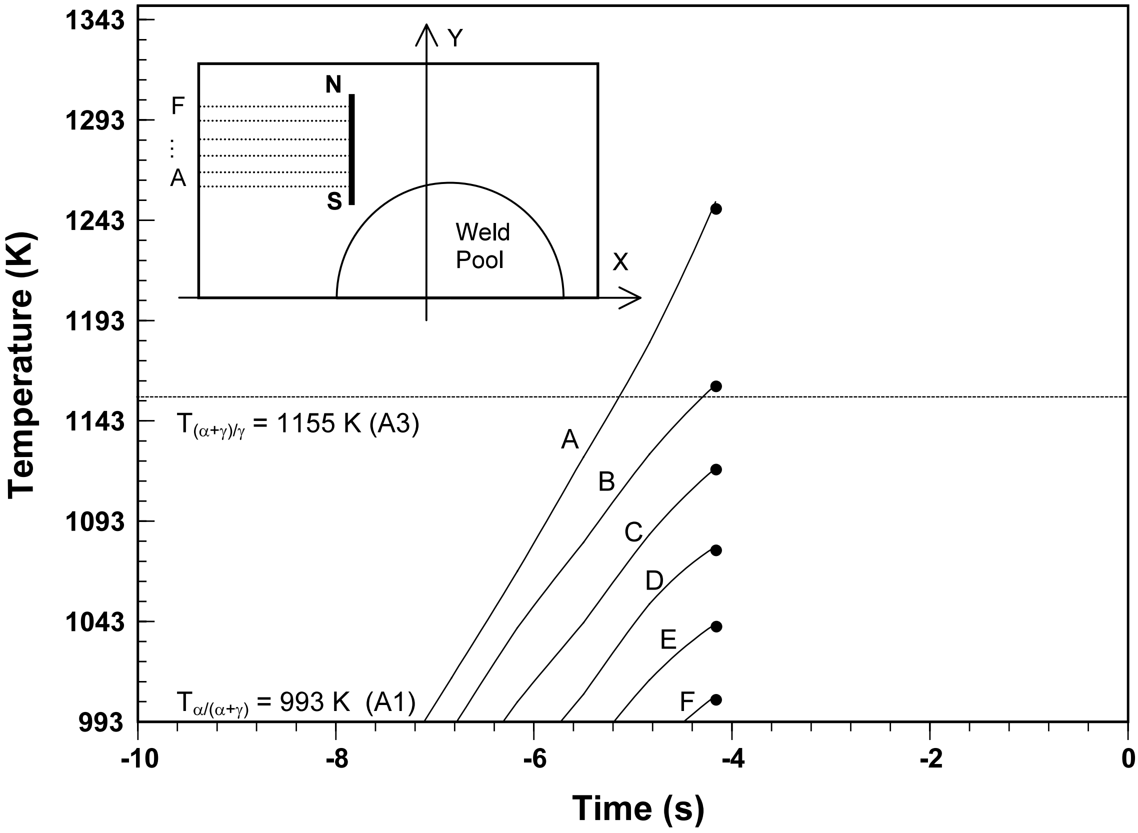

Fig. 11. Calculated thermal cycles at different locations along the monitoring line NS ($x = -2.5$ mm). Distances from weld centerline: A, 5.25 mm; B, 5.5 mm; C, 5.75 mm; D, 6.0 mm; E, 6.25 mm; and F, 6.5 mm. The temperatures indicated by the solid circles were reached when the distance between the heat source and the line NS was 2.5 mm.

Table 3
Phase fractions of austenite measured from the SRXRD phase map at $x = -2.5$ mm for various values of y [10]

Location		Thermal cycle	Temperature (K)	Phase fraction of austenite
X (mm)	Y (mm)			
−2.5	5.25	A	1254	0.903
−2.5	5.50	B	1163	0.763
−2.5	5.75	C	1115	0.276
−2.5	6.00	D	1079	0.130
−2.5	6.25	E	1041	0.052
−2.5	6.50	F	1008	0.008

The thermal cycles A through F are shown in Fig. 11.

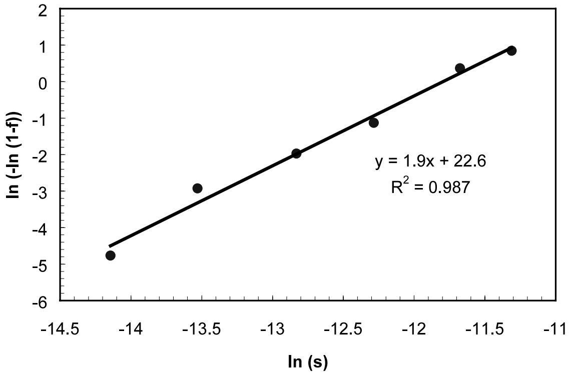

Fig. 12. The linearized JMA plot used to extract the JMA kinetic parameters.

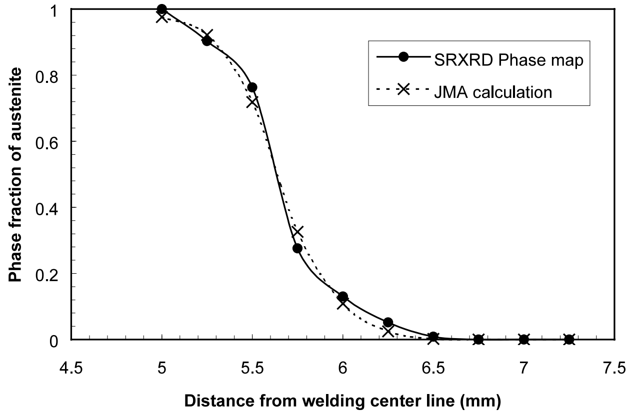

Fig. 13. Comparison of calculated and experimental γ phase fractions during α→γ transformation at different locations along the line NS shown in Fig. 11.

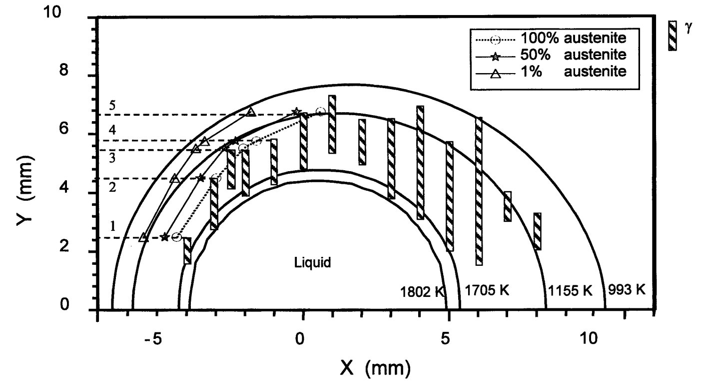

Fig. 14. Real-time SRXRD phase distribution maps for single γ-phase region. The superimposed isotherms were calculated from the 3-D heat transfer and fluid flow model. The extent of α→γ transformation was calculated by the combination of the modified JMA equation and computed thermal cycles 1–5, which are shown in Fig. 8. Good agreement is observed between the JMA calculated (indicated by the 100% austenite profile) and SRXRD measured (end of vertical bands) (α + γ)/γ phase boundary on the heating side of the weld.

was calculated using Eq. (7) and the respective temperature versus time plot shown in Fig. 11. The summation of s according to Eq. (7) started from A1 temperature since no α→γ transformation takes place below this temperature. The summation ended at temperatures shown by the solid circles in Fig. 11. The linearized JMA data of $\ln\{-\ln(1-f)\}$ versus $\ln s$ are plotted in Fig. 12, and the values of the slope and the intercept of the plot were determined from a linear regression analysis. The values of n and k_0 were found to be 1.9 and 1.33×10^5, respectively. For the diffusion-controlled growth, this value of JMA time exponent, $n = 1.9$, indicates that the nucleation rate of γ decreases with time [30]. This result is consistent with the sequence of events during α→γ transformation. The γ grains first nucleate at ferrite/cementite interface in the existing pearlite colonies. As cementite particles dissolve in the neighboring γ grains, other sites, such as α grain boundaries and secondary particles, may still be active for the further nucleation of γ, but the nucleation rates at these sites may be lower than those within the pearlite colonies. After the γ nucleates, the growth occurs by a diffusion-controlled mechanism [20].

Using the calculated JMA parameters, a consistency check was performed to ensure that the values of n, k_0 and Q could produce the correct values and shapes of the γ fraction versus distance plot along the line NS from $y = 5.25$–7.25 mm at $x = -2.5$ mm. Fig. 13 shows the calculated and experimental phase fractions of γ along NS. Good agreement between the calculated results and the experimental data indicates the consistency of the calculations.

The calculated JMA parameters were also used to calculate the complete (α + γ)/γ phase boundary. As discussed earlier, determination of this phase boundary requires both the kinetics of α→γ transformation and the computed temperature profiles at various locations. The thermal cycles along various paths parallel to the welding directions indicated in Fig. 14 are determined. They are presented in Fig. 8 as thermal cycles 1 through 5. With the knowledge of the JMA kinetic parameters and thermal cycles, the extent of α→γ transformation along these paths were quantitatively calculated using Eq. (4). The location where the calculated phase fraction of austenite is equal to 1, 50 and 100% are shown in Fig. 14. In this figure, the dashed line for 100% austenite represents the calculated (α + γ)/γ boundary for the specific welding conditions used in the present investigation. It is found that the calculated (α + γ)/γ boundary agrees well with that determined from the SRXRD phase map. This agreement provides an independent confirmation of the JMA parameters determined from the phase fractions along NS.

The kinetic parameters were also used to calculate the extent of α→γ transformation along a direction parallel to the fusion line at $y = 4.4$ mm. The thermal cycle used in the calculation corresponds to the thermal cycle FL in Fig. 8. The computed γ fraction at various locations along $y = 4.4$ mm is shown in Fig. 15. The computed start and finish positions of $\alpha \rightarrow \gamma$ transformation along the fusion line were found to be $x = -4.9$ and -3.0 mm, respectively, while the start and finish positions determined from the SRXRD phase map were $x = -4.7$ and -2.9 mm [10], respectively. The good agreement between the experimental and calculated results shows that the JMA kinetic parameters accurately describe the kinetics of $\alpha \rightarrow \gamma$ transformation in AISI 1005 steel. Thus, the kinetics of the $\alpha \rightarrow \gamma$ transformation in AISI 1005 steel during heating can be predicted using the modified JMA equation and the computed thermal cycles.

Two of the kinetic parameters in Eq. (4), i.e. k_0 and n depend on the initial microstructure of the base metal. In particular, recent calculations show that the kinetics of $\alpha \rightarrow \gamma$ transformation depend on the geometry of the α and carbide phases in the microstructure [19,31]. In view of the lack of quantitative kinetic data in the literature, the extent of dependence of the kinetic parameters on the initial microstructure cannot be determined at this time. The lack of kinetic data emphasize the need for quantitative investigations on this topic and suggest that the parameter values obtained in this investigation should be used carefully, paying particular attention to the starting microstructure indicated in Fig. 2.

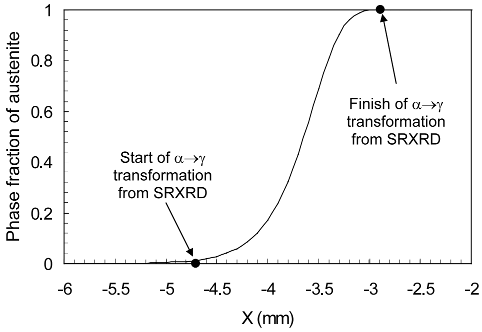

Fig. 15. Calculated phase fraction of γ along the fusion line at $y = 4.4$ mm. The start and finish positions of $\alpha \rightarrow \gamma$ transformation were determined from the SRXRD phase map [10].

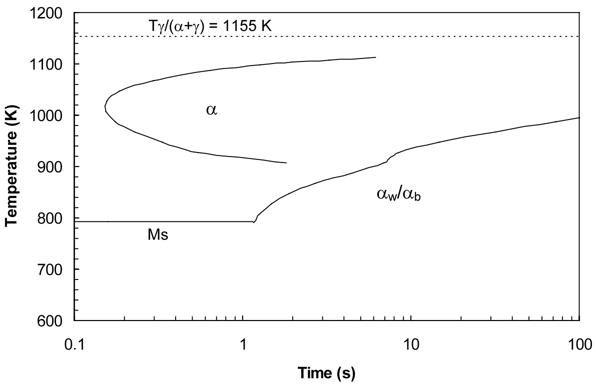

Fig. 16. Calculated TTT diagram for the AISI 1005 steel welds. The symbols α, α_w, α_b and Ms represent allotriomorphic ferrite, Widmanstatten ferrite, bainite and martensite, respectively. In this figure time equal to zero refers to a temperature of 1273 K.

Table 4

Comparison between the calculated and experimental volume fractions of microconstituents in the fusion zone

	Experimental volume fraction (%)	Calculated volume fraction (%)
V_α	31.6 ± 3.7	35
V_W	59.0 ± 2.2	54
V_o	9.4 ± 3.3	11

The symbols V_α, V_W and V_o represent the volume fractions of allotriomorphic ferrite, Widmanstatten ferrite and other microconstituents, respectively.

4.3.3. Transformation of austenite during cooling in the FZ

The computed TTT diagram for the AISI 1005 weld metal using the existing model [13–15] is shown in Fig. 16. The diagram consists of two curves. The upper C shaped curve at higher temperatures represents the austenite to allotriomorphic ferrite transformation by diffusion, while the one at lower temperatures represents displacive transformations, such as austenite to Widmanstatten ferrite and bainite [6,13–15]. The $\gamma \rightarrow \alpha$ transformation during cooling exhibits the classical C curve kinetic behavior due to the interaction of two opposing effects, diffusion rates decrease with decreasing temperature while the chemical driving force for the transformation increases. The martensite transformation is represented by a horizontal line, which indicates that the transformation is independent of time. It should be noted that the initially solidified regions are depleted of solute and, in principle, these regions are first transformed to ferrite. However, due to the low carbon and alloy concentrations in the AISI 1005 steel, the difference between the TTT curves for solute-depleted and bulk regions was very small. Therefore, only the TTT curve for the bulk region was considered. Fig. 17 shows the CCT diagram computed from the TTT diagram based on the Scheil additive rule [32]. The superimposed cooling curve was taken along the thermal cycle at $y = 2.5$ mm, i.e. thermal cycle 2 in Fig. 8. It was found that the cooling curve intercepts both the replacive and displacive curves. Thus, both allotriomorphic and Widmanstatten ferrites are expected to form.

The volume fractions of microconstituents in the FZ calculated using the phase transformation model and the computed thermal cycle at $y = 2.5$ mm are shown in Table 4. The calculated transformation start temperatures are presented in Table 5. From Table 4 to Table 5 it is observed that for the cooling curve shown in

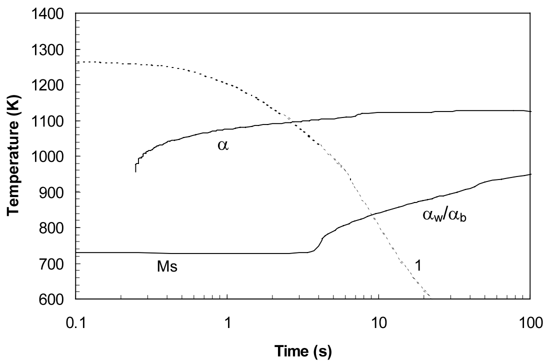

Fig. 17. Calculated CCT diagram for the AISI 1005 steel welds. The superimposed cooling curve 1 corresponds to a location of $y = 2.5$ mm. The symbols α, α_w, α_b and Ms represent allotriomorphic ferrite, Widmanstatten ferrite, bainite and martensite, respectively. In this figure time equal to zero refers to a temperature of 1273 K.

Fig. 17, the γ to allotriomorphic ferrite transformation starts at 1089 K and 35% of γ transforms into allotriomorphic ferrite. At 863 K, Widmanstatten ferrite transformation begins and an additional 54% of the γ transforms to Widmanstatten ferrite. The remaining 11% austenite transforms into bainite and martensite. Good agreement was found between the calculated and the experimental volume fractions of allotriomorphic and Widmanstatten ferrites in the weld metal. The results indicate significant promise for understanding microstructure evolution in the FZ of AISI 1005 steel during welding by a combination of phase transformation model and transport phenomena based calculation of thermal cycles.

5. Summary and conclusions

Microstructure evolution during GTA welding of AISI 1005 steel was studied experimentally by the SRXRD technique and modeled using a combination of transport phenomena and phase transformation kinetics. The following conclusions can be made from the investigation. The geometry of the FZ and HAZ, $(\delta + \gamma)$/liquid boundary, and the $\alpha/(\alpha + \gamma)$ phase boundary on the heating side of the weld predicted from a 3-D heat transfer and fluid flow model were in good agreement with the corresponding experimental results. However, the prediction of the $(\alpha + \gamma)/\gamma$ boundary requires consideration of phase transformation kinetics in addition to the thermal model. The JMA kinetic parameters for $\alpha \rightarrow \gamma$ phase transformation in AISI 1005 steel were determined from the experimental SRXRD phase map. The kinetics of the $\alpha \rightarrow \gamma$ phase transformation could be satisfactorily predicted by the combination of the modified JMA equation and calculated thermal cycles. The JMA time exponent of 1.9 is consistent with the fact that during the $\alpha \rightarrow \gamma$ phase transformation in AISI 1005 steel, the nucleation rate of γ phase from the α matrix decreases with time. The growth of γ grain is controlled by the diffusion mechanism. The FZ microstructure in AISI 1005 steel consisted predominantly of allotriomorphic and Widmanstatten ferrites and small amounts of other microconstituents. An existing phase transformation model and the computed thermal cycles were used to calculate the volume fractions of microconstituents in the FZ. Good agreement was found between the calculated and the experimental volume fractions of allotriomorphic and Widmanstatten ferrites in the weld metal. The determination of kinetic parameters in the JMA equation for the $\alpha \rightarrow \gamma$ phase transformation in the HAZ, insight about the nucleation mode of austenite from the ferrite matrix and the quantitative understanding of the microstructure evolution in the FZ during GTA welding of AISI 1005 steel could only be achieved by the combination of experiments and modeling.

Table 5
Calculated start temperatures of austenite to different phases during cooling in the fusion zone

Transformation	Start temperature (K)
Allotriomorphic ferrite	1089
Widmanstatten ferrite	863
Martensite	724

Acknowledgements

The Penn State portion of this research was supported by a grant from the US Department of Energy, Office of Basic Energy Sciences, Division of Materials Sciences, under grant number DE-FGO2-01ER45900. The LLNL portion of this research was performed under the auspices of the US Department of Energy, Lawrence Livermore National Laboratory, under Contract No. W-7405-ENG-48. The authors thank Todd A. Palmer of LLNL for his interest in this work. The authors are grateful to Professor H.K.D.H. Bhadeshia for help with the microstructure calculations.

Appendix A. Phase transformation model used to calculate $\gamma \rightarrow \alpha$ phase transformation in the FZ

Assumptions in the model

In low alloy steel welds, solidification involves the epitaxial growth of δ at the fusion boundary. The final δ grains have an anisotropic columnar morphology, with their major axes lying along the direction of maximum heat flow [33]. On further cooling, γ grains nucleate at the δ grain boundaries and grow along these boundaries. The resulting γ grains closely resemble the

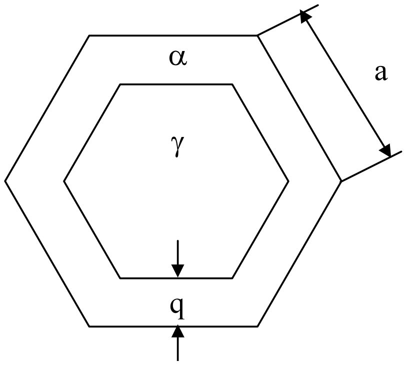

Fig. 18. Assumed shape of an austenite grain, where γ is austenite grain, α is allotriomorphic ferrite layer, q is the thickness of allotriomorphic ferrite layer, and a is the side length of hexagonal austenite grain.

original δ grain morphology. Thus, the morphology of the γ grains in the FZ can be assumed to be represented as a honeycomb of hexagonal prisms with height c and cross-section side length a, as shown in Fig. 18 [34]. The c axes of the prisms are parallel to the direction of the maximum heat flow. The side length, a, was measured along the longitudinal sections.

It will be shown later in this appendix that the prior austenite grain size is necessary for the quantitative calculation of volume fractions of allotriomorphic and Widmanstatten ferrites during transformation of austenite. In order to reveal the prior austenite grain structure, the FZ of welded samples was sectioned along the longitudinal direction, as shown in Fig. 1. The representative microstructure etched by a saturated picral solution [16] is shown in Fig. 19, where the average austenite side length, a, was measured by the lineal intercept method as:

$$a = \frac{2 \times L_1}{\pi \times \cos(30°)} \tag{A.1}$$

where L_1 is the mean lineal intercept measured randomly on longitudinal sections [26,34]. The measured value of the average austenite side length is an important parameter in the calculation of ferrite growth rate in the model.

In the calculations that follow, it is assumed that paraequilibrium exists at the γ/α interface during transformation. Paraequilibrium is constrained phase equilibrium when a phase change is so rapid that one or more components cannot redistribute within the phase in the available time scale [13–15]. The paraequilibrium condition implies that the substitutional solute/iron atom ratio remains constant everywhere, allowing the transformation to be controlled by the diffusion of carbon. The substitutional alloying elements can only influence kinetics through their effect on the carbon concentration and activity at the α/γ interface [13–15].

Calculation of TTT and CCT diagrams

The TTT curves in the model are classified into two C curves, the one at higher temperature representing replacive transformations, and that at lower temperature representing displacive transformations. The incu-

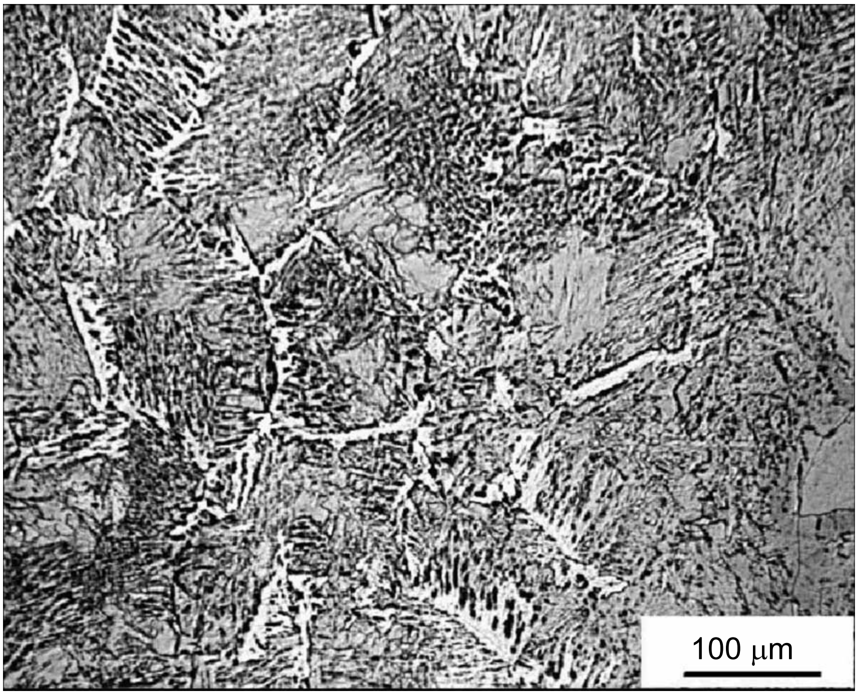

Fig. 19. Optical micrograph of the FZ, etched in saturated picral solution. The grain boundary allotriomorphic ferrite outlines the prior austenite columnar grains in white.

bation times for both replacive and displacive transformations are calculated by Russell's expression [35,36]:

$$\tau = T^a \times (\Delta G_{\max})^b \times \exp\left(\frac{c}{T}\right) \times d \tag{A.2}$$

where τ is the incubation time for a transformation, T is the temperature, $\Delta G_{\max}$ is the maximum driving force for nucleation and a, b, c and d are constants. The details of calculation of $\Delta G_{\max}$ and determination of constants a, b, c, and d are given in [13].

The CCT diagram can be calculated from the corresponding TTT diagram based on Scheil additive rule [32]:

$$\int_0^t \frac{\mathrm{d}t}{t_a(T)} = 1 \tag{A.3}$$

where $t_a(T)$ is the incubation time to a specified stage on a TTT diagram for isothermal reactions, t is the time to that stage for the non-isothermal reactions, and dt is the time interval at temperature T. In this procedure, the total time to reach a specified stage of transformation for non-isothermal reactions is obtained by adding the fractions of the time to reach this stage isothermally until the sum reaches unity.

Calculation of phase volume fractions

When the weld metal cools to a temperature below Ae3, austenite begins to transform into a layer of allotriomorphic ferrite that grows from the prior austenite grain boundary by diffusion. The start temperature for this transformation is determined from the interception temperature of the cooling curve and upper C curve in the CCT diagram, as shown in Fig. 17. The completion temperature for the allotriomorphic ferrite transformation is taken from the interception temperature of the cooling curve with the lower C curve, because below this temperature displacive transformations are assumed to be kinetically favored. At this point, the growth of allotriomorphic ferrite ceases and gives way to displacive transformations. Under the paraequilibrium assumption, the growth rate of allotriomorphic ferrite is controlled by diffusion of carbon in the austenite ahead of the moving allotriomorphic ferrite/austenite interface. The thickness of the allotriomorphic ferrite layer can be calculated by the following parabolic thickening relationship [13–15]:

$$q = \int_{T_1}^{T_h} 0.5\alpha_1 t^{-0.5}\,\mathrm{d}t \tag{A.4}$$

where q is the thickness of the allotriomorphic layer, t is the time, T_h and T_l are the start and finish temperatures of the transformation, respectively, and α_1 is the one-dimensional (1-D) parabolic thickening rate constant. Based on the area that allotriomorphic ferrite occupies in the hexagonal cross section of austenite grain, as shown in Fig. 18, the volume fraction of allotriomorphic ferrite (V_α) can be calculated as [13–15]:

$$V_\alpha = \frac{[2q\tan(30°)(2a - 2q\tan(30°))]}{a^2} \tag{A.5}$$

where V_α is the volume fraction of allotriomorphic ferrite, q is the thickness of allotriomorphic ferrite, a is the side length of austenite.

The austenite to Widmanstatten ferrite transformation is a paraequilibrium displacive transformation with the growth rate controlled by the combination of carbon diffusion and an invariant-plane strain (IPS) change [3,6]. Based on the area that Widmanstatten ferrite occupied in the hexagonal cross section of austenite grain after the formation of the allotriomorphic ferrite, the volume fraction of Widmanstatten ferrite (V_w) is calculated by [13–15]:

$$V_w = C_4 G\left[\frac{2a - 4q\tan(30°)t_2^2}{(2a)^2}\right] \tag{A.6}$$

where C_4 is a constant independent of alloy composition, G is the lengthening rate of Widmanstatten ferrite, a is the side length of austenite, q is the thickness of the allotriomorphic ferrite layer and t_2 is the time available for the formation of Widmanstatten ferrite.

The volume fraction of microconstituents other than allotriomorphic and Widmanstatten ferrites, V_o, is calculated from the mass conservation equation:

$$V_o = 1 - V_\alpha - V_w \tag{A.7}$$

where V_α and V_w are volume fractions of allotriomorphic ferrite and Widmanstatten ferrite, respectively.

References

[1] Ø. Grong, Metallurgical Modelling of Welding, second ed., The Institute of Materials, London, 1997.

[2] K. Easterling, Introduction to the Physical Metallurgy of Welding, second ed., Butterworth Heinemann, Boston, 1992.

[3] L.-E. Svensson, Control of Microstructures and Properties in Steel Arc Welds, CRC Press, Boca Raton, 1994.

[4] R. Mancini, C. Budde, Acta Mater. 47 (1999) 2907.

[5] R.C. Reed, T. Akbay, Z. Shen, Mater. Sci. Eng. A256 (1998) 152.

[6] S.J. Jones, H.K.D.H. Bhadeshia, Acta Mater. 45 (1997) 2911.

[7] J.H. Valentich, Tube Type Dilatometers: Applications From Cryogenic to Elevated Temperatures, Instrument Society of America, Research Triangle Park, NC, 1981.

[8] J.W. Elmer, J. Wong, M. Fröba, Metall. Mater. Trans. A27 (1996) 775.

[9] J.W. Elmer, J. Wong, T. Ressler, Scr. Mater. 43 (2000) 751.

[10] J.W. Elmer, J. Wong, T. Ressler, Metall. Mater. Trans. A32 (2001) 1175.

[11] K. Mundra, T. DebRoy, K. Kelkar, Numer. Heat Transfer 29 (1996) 115.

[12] K. Mundra, J.M. Blackburn, T. DebRoy, Sci. Technol. Welding Joining 2 (1997) 174.

[13] H.K.D.H. Bhadeshia, Metal Sci. 16 (1982) 159.

[14] H.K.D.H. Bhadeshia, L.-E. Svensson, B. Gretoft, Acta Metall. 33 (1985) 1271.

[15] H.K.D.H. Bhadeshia, L. -E. Svensson, in: H. Cerjak, K.E. Easterling (Eds.), Mathematical Modeling of Weld Phenomena, Institute of Materials, London, 1993, pp. 109–180.

[16] L.E. Samuels, Light Microscopy of Carbon Steels, ASM International, Materials Park, OH, 1999.

[17] International Institute of Welding (IIW), Weld. World 29 (1991) 160.

[18] S.V. Patankar, Numerical Heat Transfer and Fluid Flow, Hemisphere, Washington DC, 1980.

[19] T. Akbay, R.C. Reed, C. Atkinson, Acta Metall. Mater. 47 (1994) 1469.

[20] M. Hillert, K. Nilsson, L.-E. Törndahl, J.I.S.I. 209 (1971) 49.

[21] A. Roosz, Z. Gacsi, E.G. Fuchs, Acta Metall. 31 (1983) 509.

[22] F.G. Caballero, C. Capdevila, C. García de Andrés, Metall. Mater. Trans. A32 (2001) 1283.

[23] S.K. Nath, S. Ray, V.N.S. Mathur, ISIJ Int. 34 (1994) 191.

[24] Z. Qi, W. Yan, Trans. Metal Heat Treatment (People's Republic of China) 13 (1992) 25.

[25] P. Kruger, J. Phys. Chem. Solids 54 (1993) 1549.

[26] Z. Yang, J.W. Elmer, J. Wong, T. DebRoy, Welding J. 79 (2000) 97s.

[27] Z. Yang, T. DebRoy, Sci. Technol. Welding Joining 2 (1997) 53.

[28] L. -E. Svensson, B. Gretoft, H.K.D.H. Bheadeshia, Scand. J. Metall. 15 (1986) 97.

[29] Z. Yang, T. DebRoy, Metall. Mater. Trans. B30 (1999) 483.

[30] J.W. Christian, The Theory of Transformations in Metals and Alloys, Part I, second ed., Pergamon, Oxford, UK, 1975.

[31] H.K.D.H. Bhadeshia, Bainite in Steels, second ed., Institute of Materials, London, 2001.

[32] M. Takahashi, H.K.D.H. Bhadeshia, Mater. Trans. 32 (1991) 689.

[33] G.J. Davies, J.G. Garland, Int. Metall. Rev. 20 (1975) 83.

[34] H.K.D.H. Bhadeshia, L.-E. Svensson, B. Gretoft, J. Mater. Sci. 21 (1986) 3947.

[35] K.C. Russell, Acta Metall. 16 (1968) 761.

[36] K.C. Russell, Acta Metall. 17 (1969) 1123.